Optimization and High Flow on Vein Model System for Hemodynamic Characterization in Hemodialysis Population

By

Maren Klineberg

submitted as a THESIS toward the degree of BACHELOR OF SCIENCE

in

BIOLOGICAL SCIENCES

in

THE COLLEGE

of

THE UNIVERSITY OF CHICAGO

Approved:

Signature of thesis adviser/date: , 5/5/2023

Name of thesis adviser: Anindita Basu

Signature of faculty reader #1/date: May 10, 2023

Name of faculty reader #1: Jay Koyner

Signature of faculty reader #2/date: May 11, 2023

Name of faculty reader #2: Sam Armato

Abstract

Thrombosis and stenosis are major complications for dialysis patients. Previous research posits that areas of low Wall Shear Stress (WSS) influence dialysis complication risk in patients. Fluidic devices that replicate vein geometries of the cephalic arch of those with brachiocephalic arteriovenous fistulas (AVF) allow for characterization of WSS and flow behavior in a patient specific way. This study reviews design changes made to the fluidic devices in order to recreate pathologic flow rates on chip (from 20 mL/min to 300 mL/min), along with time series imaging of pathologic flow and resultant WSS. These changes revealed flow transitions from laminar to turbulent as flow rates increased. Interestingly, this transition from laminar to turbulent flow occurs at different flow-rates in different regions of the device, and is strongly influenced by overall device geometry as well as local topography of the wall surface.

WSS profiles were generated for five fluidic models at a flow rate of 300 mL/min to model. This includes an idealized 9 mm diameter cephalic arch model in AVF patients, and four total patient specific models: two patients, each with a model at 3 and 12 months after AVF creation. These profiles recapitulate WSS values expected under pathologic flow while capturing systematic changes in WSS over time due to vein remodeling, in a patient-specific manner. These results will help understand overall changes in hemodynamics and WSS in patients under dialysis treatment and why certain patients are prone to AVF complications.

Introduction

Dialysis

In 2020, there were nearly 786,000 people with End Stage Renal Disease (ESRD) in the US according to the United States Renal Data System Annual Report. ESRD is defined as when the kidney has under 10 - 15% function. 71% of those people require frequent dialysis treatment in order to live[1]. Hemodialysis, the most common type of treatment, is provided multiple times a week using an external artificial filtration system to filter the patients' blood of uremic toxins, such as urea, creatine, β2-microglobulin, α1-macroglobulin, indoxyl sulfate (IS), and p-cresyl sulfate (PCS), in lieu of failing kidneys[2–6]. Needles connect the patient's vein to the hemodialysis machine for purification. Treatment is lifesaving, but it is still incredibly difficult on patients. Patients spend more than the equivalent of a full workday under hemodialysis treatment each week: 4 hours per session, 3 sessions per week[1].

Hemodialysis treatment cannot be done on normal veins because they are not large or strong enough to withstand the high blood flow rates needed to complete treatment. Therefore, an access point must first be created. Accesses promote vein remodeling to make it large enough and strong enough to undergo treatment and assist inserting the needles that connect the patient to the dialysis machine. The two most common types of dialysis access are called fistulas and grafts. An arteriovenous fistula (AVF) is where a vein is surgically connected to an artery. Vein remodeling occurs in response to the increased blood flow from the artery. Successful remodeling is also referred to as fistula maturation. A graft is a fistula created with artificial tubing. Grafts thrombose more often than fistulas due to the lack of an endothelium, but are also easier to save because of

that lack. It is typically done after a regular fistula has failed due to complications, or if the veins are not large enough.

Dialysis Complications

Frequently complications occur that prevent dialysis treatment from continuing. The most common issues are thrombosis and stenosis[7,8]. Thrombosis refers to blood clot formation, while stenosis refers to when the vein remodeling causes the vein wall to thicken and thus narrow the vein lumen over time. Stenosis may also result in increased fluid retention, AVF failure, elevated venous and arterial pressures, increased pain and bleeding during dialysis treatment[9]. Mechanical stretch and shear stress promote vein remodeling[10]. Other diseases such as atherosclerosis and hypertension are also a result of mechanical forces on the endothelial cells of the vein wall[11,12]. The field currently hypothesizes that thrombosis may similarly be caused by damage to the endothelium. Dialysis complications like thrombosis and stenosis often occur in conjunction and prevent blood from easily flowing through the vein and require surgical intervention to fix. This creates a large problem for the patient, as they cannot receive the necessary dialysis treatment until the complication is resolved. Medical intervention must be made as quickly as possible for optimal outcomes[9].

Thrombosis and stenosis are serious health problems, but they also create financial strain on patients[13]. In 2012, Medicare estimated that it spent $90,000 per patient per year on hemodialysis treatment, and in 2017 Medicare reimbursement rates show the average index cost of a stent, a common treatment for stenosis, costs nearly $10,000 when performed at a hospital outpatient center[14,15].

Brachiocephalic AVFs specifically fail due to cephalic arch stenosis in 77% of patients over five years[16,17]. Thrombosis or aneurysms cause brachiocephalic AVFs in 6.25% of patients to fail over six months[18]. However, there is currently no way to identify who is at risk for these complications. Due to the inability to predict risk, little preventative care is possible. Standard of care tends to be reactive, not proactive. If reliable predictions of poor patient outcomes could be made, preventative care could stop invasive and expensive treatment from being needed, greatly improving the quality of life for these patients.

Arteriovenous Fistulas

Fistulas can be created in both the arm and the leg. The fistula mentioned throughout this paper for experimentation is a brachiocephalic fistula, which make up 2/3 of the AVF placements[7]. This is a fistula that connects the brachial artery and the cephalic vein, located in the upper arm right above the elbow.

The cephalic arch in the shoulder, where the cephalic vein connects to the axillary vein, was observed to be a common site for thrombosis and stenosis in dialysis patients[16,19,20]. It was hypothesized that this is due to the bend geometry of the area influencing blood flow characteristics to increase risk via damage to the endothelium or by concentrating prothrombotic factors.

Wall Shear Stress

One way of measuring how the vein geometry impacts the hemodynamics of the vein is wall shear stress. Wall shear stress (WSS) in this context is the force the blood creates on the endothelial cells lining the vein wall. It is mathematically derived from the equation: $\tau = \mu \frac{du}{dy}$, where μ is dynamic viscosity, y is distance from the wall, and u is velocity. WSS is typically

indirectly calculated using Poiseuille's equation: $Q = -\frac{\Delta P \pi R^4}{8\mu L}$ with flow rate Q, viscosity μ, pipe length L, pipe radius R, and pressure difference ΔP[21]. Viscosity, velocity, and vessel diameter are measured from bloodwork and ultrasounds. However, this equation assumes perfect tubular geometry which does not match the geometry of patient veins, creating inherent error in the resulting values. Sufficient WSS has been found to promote proper endothelial growth and function, proper AVF maturation, but when too high it is associated with vascular inflammation and can even detach the endothelium when over 40 N/m^2 [22–27]. Previous research finds areas of low WSS correspond to increased risk of neointimal hyperplasia, atherosclerosis plaque development, thrombosis, and stenosis in veins [12,19,22,27–29]. Low WSS may be caused by the vein geometry or by complex blood flow behavior such as recirculation pools or turbulence. Turbulence is extremely chaotic flow behavior and is complicated and unsolved but can be partially predicted[30]. It has been strongly connected to vascular damage, though others posit that turbulence is a normal part of physiologic flow[31,32]. Though it is known broadly how WSS impacts veins, not enough about the specific ranges for risk are known, especially in humans. This makes it currently difficult to use clinically and differentiate which patients are at risk.

Past Work

This is not the first vein model used; several ex vivo vein models have been utilized to understand how veins respond to stimuli. One of the earliest examples of this is a model that uses postmortem veins to study atherosclerosis where 12 adult human bifurcations taken from autopsies and were distended and fixed to reflect their normal shape and configuration[33]. Laser-Doppler anemometry was used to determine the WSS and flow rate in these models at different Reynolds numbers. They found that intimal thickening and atherosclerosis occurred more often in areas of

relatively low WSS. However, areas that had moderate to high WSS with unidirectional and axially aligned flow were much less prone to atherosclerosis. Another ex vivo vein model used porcine saphenous veins in different hemodynamic environments to understand which factors are required for remodeling[34,35]. Similar to the previously described ex vivo model, it found that higher WSS corresponded to less intimal thickening, while lower WSS was associated with more intimal thickening. However, it also found that average pressure directly correlated with medial area: veins with higher pressure had more medial area, while those exposed to lower pressure had less medial area. The results suggest that pressure and WSS both independently regulated vein remodeling, but pulseatile flow was not necessary for remodeling. While these models can teach us much about the nature of veins, these ex vivo models cannot be adapted for patient-specific study or clinical use for living patients.

Computational vein models are also common. One such model uses a computational simulation of an arteriovenous graft to understand stenosis[36]. The model has three different angles for the anastomosis, where the artery and vein meet, and analyzed flow characteristics including WSS to identify which was least likely to undergo stenosis. The higher anastomosis angle in the venous anastomosis caused stenosis in the simulation. Another computational model was used to study the best needle placement during dialysis[37]. This simulation showed that high blood flow rates exiting the venous needle caused high WSS and damaged the endothelium, but shallow needle angles, a blood flow rate of approximately 300 ml/min, and placement of the needle tip away from the vein wall could lower the risk. Another model compared the hemodynamics before and after stent placement to treat stenosis in a dialysis patient[38]. This simulated model found that stent placement lowered the average pressure, WSS, and flow rate, and decreased turbulence in the vein. Another model used a MRI-based computational fluid dynamics on mice AVFs to

generate hemodynamic profiles[39]. The model found that flow velocity, WSS, spatial WSS gradient, and oscillatory shear index all increased after AVF installation.

Another group created an in vitro vein model to study hemodynamics in an AVF[40]. The vein model was connected to a heart simulator. The AVF configuration resulted in a decrease in distal pressure and flow compared to a baseline without an AVF. A configuration with distal revascularization saw no change in distal pressure with an increase in distal flow, while the configuration with distal revascularization and interval ligation saw an increase in both distal pressure and flow. The researchers suggest that further testing to help identify ideal AVF placement and allow study of treatments for ischemic steal, an AVF complication where the blood decreases or reverses through the artery. A generalized in vitro model will help avoid some of the limitations of computational models but does not allow the clinical relevance of a patient specific model.

The patient specific vein models described in this study could help individualize hemodialysis patient care and provide greater understanding of the hemodynamics in dialysis veins. Previous work on this subject by us includes a longitudinal study on patient outcomes, a purely computational version of the model, and a previous version of the fluidic model operating at physiologic blood flow rates[28,41,42]. The longitudinal study covered 40 ESRD patients with bracchiocephalic AVFs on dialysis for three years or until stenosis. This study showed 40% of the patients lost dialysis access due to thrombosis, 32 developed stenosis, and for 26 patients the stenosis site corresponded to areas of low WSS during fistula maturation. In addition to increased risk of thrombosis and stenosis, the patients also experienced areas of low WSS, pulsatile flow, and increased blood flow viscosity in the cephalic vein[28]. This finding is supported by other studies[43–47]. Our previous computational model developed the procedure for creating 3D

reconstructions of patient veins from intravascular ultrasounds and venograms at two timepoints of 3 and 12 months after AVF installation [41]. These computational models used COMSOL Multiphysics (COMSOL Inc.), version 5.5, Physics simulation software to simulate blood flow in the reconstructed veins to generate WSS profiles[48]. To make physical models, the computational reconstructions were then 3D-printed and used to create physical replicas of the patient veins[42]. The physical models at physiologic flow rates demonstrated the proof of concept and validation for the models in this study. It was the first to directly calculate WSS in the cephalic arch. Direct measurement does not require any previous assumptions or biases and are likely more accurate to patients. This study incorporates pathologic levels of elevated flow to these physical models. It is a step towards aqquireing patient-specific data needed to better understand how WSS impacts veins and patient outcomes and will allow patient specific treatment.

Materials and Methods

Three-Dimensional (3D) Model

A 3D computational model was reconstructed using the intravascular ultrasound (IVUS) and venogram from each dialysis patient at two time points, 3 and 12 months post AVF creation. Images were compiled into a 3D computational model. More detailed description of the procedure can be found in previous papers [41,42].

Fabrication

Each 3D computational model, as well as a smooth idealized physiologic and pathologic model, had inlet and outlet connectors added using Trimble SketchUp and was turned into a 3D printing file. Each file was then printed out using a water-soluble filament, polyvinyl alcohol filament (PVA) with a Cura Lulzbot Taz4 3D printer. The printed mold was used to cast

polydimethylsiloxane (PDMS) made from a 9:1 ratio of base to crosslinker by weight inside a box mold. To ensure an accurate model with no bubbles, the PDMS casting was done in layers and placed in a vacuum desiccator for 30 min before curing each layer. To enclose the model completely, the first layer of PDMS was cured before the print was added. To cure the PDMS, the model was placed in an oven at 65˚C for at least 1 hour. Then the process was repeated for the additional layers. After all layers were complete, the model was autoclaved in a B4000-16 BioClave Research Autoclave at 134 °C, 30 psi while submerged in water to dissolve the PVA print. PCR foil was used to cover the top and bottom of the models to preserve their clarity and improve image quality. The number of rounds that each model must be autoclaved varies due to size and geometry, but most required 4 - 5 rounds. The end result created a 3D replica of the patient's vein cavity in a PDMS model. This model must then have tubing attached. Two 1/4 inch tubing connectors (#5117K46, McMaster-Carr) were plugged into the inlet and outlet spaces in the model. To these connectors, 10 cm sections of 1/4 inch inner diameter tubing (#5393K41 McMaster-Carr) were attached. Then to the other end of this tubing, a 1/4↔1/8 inch tubing connector (#5117K61 McMaster-Carr) was added. 13 models have been fabricated, however, only five models have been used to generate results in this study. These five models include the 9 mm idealized model, to simulate a pathologic cephalic arch without patient specific geometry or remodeling, and 3 and 12 month timepoints for the Patient 104 and Patient 96 models (Figure 1). These patient models were chosen because they are also the focus of the recent paper describing the fluidic models under physiologic flow[42].

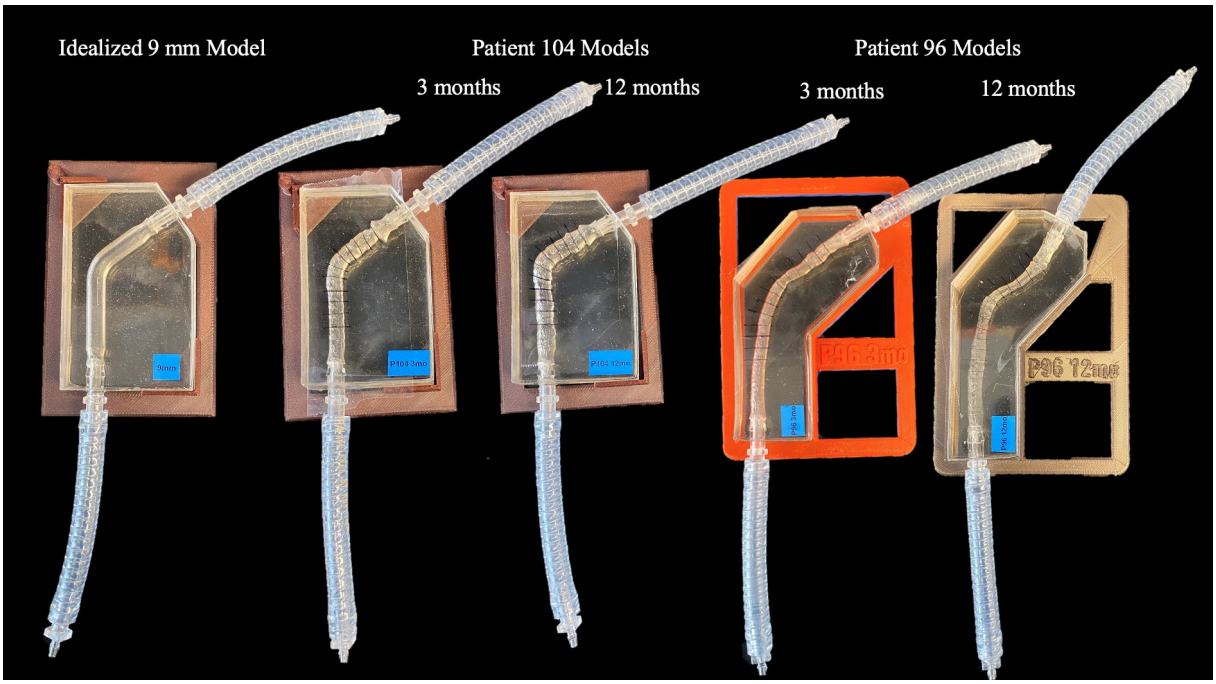

Figure 1: All of the models used in this study. Left to right is the idealized 9 mm model, the 3 and 12 month models for Patient 104, and the 3 and 12 month models for Patient 96 respectively.

Experimental Setup

To prepare for imaging and data collection, the Elveflow OB1 pressure regulator (Figure 2A) is attached to the inlet fluid reservoir container (Figure 2B) to pressurize the fluid reservoir to push the fluid through the model (Figure 2C) via the tubing pathway shown by the arrows in Figure 2 at the intended flow rate. The model is placed in a frame that ensures the model is level and secure when set in the microscope stage. The inlet tubing connector on the model was attached to 1/8 inch inner diameter inlet tubing (#5238K718 McMaster-Carr), which was connected (#5117K43 McMaster-Carr) to more 1/8 inch inner diameter tubing (#6519T16 McMaster-Carr) compatible with a fluid reservoir container filled with 400 - 600 mL of blood mimicking fluid (BMF). The outlet tubing connector on the model was attached to 1/4 inch inner diameter outlet tubing (#5393K41 McMaster Carr), which leads to an empty fluid reservoir. The BMF is a clear liquid which makes it ideal for imaging and is made of 6.3% (w/v) dextran, which matches the

average density and viscosity of the patients' blood[28]. The BMF also includes 3.5 x 10^{-6} % v/v concentration of 2 μm green fluorescent protein (GFP) Invitrogen brand fluorescent beads. The model is mounted on an Olympus IX83 fluorescent microscope and imaged on a Hamamatsu ORCA Flash4.0 camera, which allows visualization of the fluorescent beads in the images collected. During the duration of each image acquisition, known as the exposure time, the path that each fluorescent bead takes is recorded as a trace of light in the image. This allows flow behavior to be visualized as streamlines, from which we can calculate the position and velocity of the bead. The position and velocity of the bead can be used in the WSS equation to generate WSS profiles for each model.

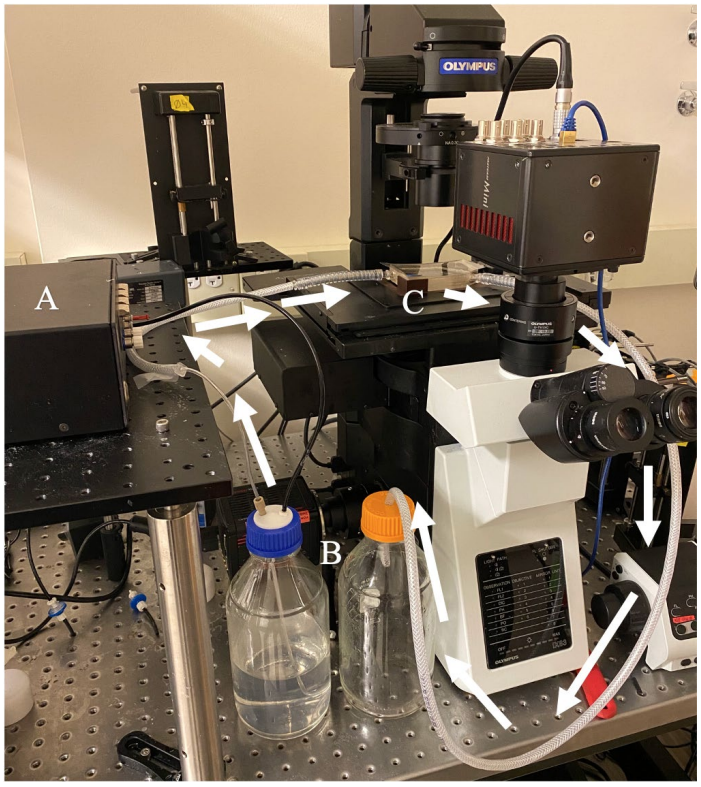

Figure 2: A) OB1 Elveflow pressure regulator. B) Inlet and outlet fluid reservoirs. C) Millifluidic device, specifically shown here is the Patient 104 3-month post AVF installation model. Additionally, the white arrows showcase the path that the flow takes through the experimental set up.

Flow Calibration

Before any flow data are collected, calibration curves for each device are made. This is done to ensure that the pressure applied to induce flow during experiments precisely corresponds to the desired flow rate. Instead of the outlet fluid reservoir, the BMF is drained from the fluidic device into a graduated cylinder. We measure the number of seconds it takes for the cylinder to fill 10 mL, or 20 mL at higher flow rates, three times at each pressure. These times are input into a Microsoft Excel spreadsheet, to calculate the flow rates produced at each applied pressure value. Flow rates measured over a range of applied pressures are plotted and fit a linear model, from which the pressure inputs necessary for each desired flow rate is calculated.

Imaging

At this stage, imaging of tracer breads under flow and data collection can commence. To prevent air bubbles in the system, the model is first primed at a low pressure, 100 mbar. Once it has been ensured that no bubbles are stuck to the wall of the model, the correct pressure input from the calibration curve equation is given to the pressure regulator. Each model was split into prebend, bend, and postbend regions. These regions were further divided into regions of interest (ROIs) on the inner and outer walls. Data was collected at each ROI while BMF and fluorescent beads flowed through the model. Imaging parameters were set using MetaMorph software.

To calculate WSS data, all images were taken at 6.4X magnification with the wall in focus. A set of 100 images were taken at each ROI. An overall magnification of 6.4X magnification was established via the 4X objective with 0.16 NA and 1.6X built-in microscope magnification.

Image datasets were taken across a wide range of flow rates (corresponding to applied pressures of 100 - 1500 mbar at 100 mbar increments, 50 images at each pressure) to visualize how the flow characteristics change as the flow rates increase. Other imaging parameters and procedural steps were identical to those for WSS imaging.

Image Processing

All raw data was saved as TIFF files, as seen in Figure 3A. The TIFF images are processed using ImageJ to obtain high-contrast streamlines and the wall outline. Image processing was performed using ImageJ, in automated steps as follows: making the images into a stack, enhancing contrast, doing an average and maximum intensity projection of all images (Figure 3B and C respectively), subtracting the average from the raw images (to remove tracer beads that were stuck to the device wall), and despeckle, resulting in Figure 3D. Then follows a manual adjustment for

brightness/contrast (Figure 3E), threshold adjustment (typically retain 0.5-0.7% highest intensity pixels) which also converts the image stack to binary (Figure 3F), and the 'analyze particles' command (typically selecting for 500-10,000 pixel length and 0-0.3 circularity) (Figure 3G), to generate high-contrast streamlines. These image analysis parameters needed to be adjusted slightly between image stacks due to the variation in image quality in each ROI. Finally, using the 'freehand select' tool to mark the wall outline from a maximum intensity projection of the first image from the raw data (Figure 3H), then using the 'image calculator' command to add the wall outline to the processed streamlines data (Figure 3I). The exact location of the vein wall is necessary to calculate WSS data, as the distance from the streamlines to the wall is one of the essential parameters in the WSS equation. The vein wall was often blurred, so this step needed to be done manually, as we did not have access to an automated method.

This final TIFF image stack after manual pre-processing was much more standardized than the raw data, allowing automated analysis of the image-stacks and calculation of WSS values. This was done by running the stacks through custom code written using Python OpenCV. This code determines the position and length of each streamline and the position of the nearest section of the vein wall. These values were then converted into velocity, by using the length of the streamline, the exposure time, and the pixel to length measurement, as well as each streamline's distance from the wall. The code calculates WSS by plugging the velocity and distance from the wall values into the WSS equation.

Then the image quality is also analyzed using the signal to noise ratio (SNR) using an ImageJ SNR plugin[49].

For the flow sweep data image processing, each image stack of 50 images was opened in ImageJ and had their brightness and contrast enhanced. Then, each stack was processed using the maximum intensity Z projection command, followed by an additional brightness/contrast adjustment. Then this data was saved as .JPEG files.

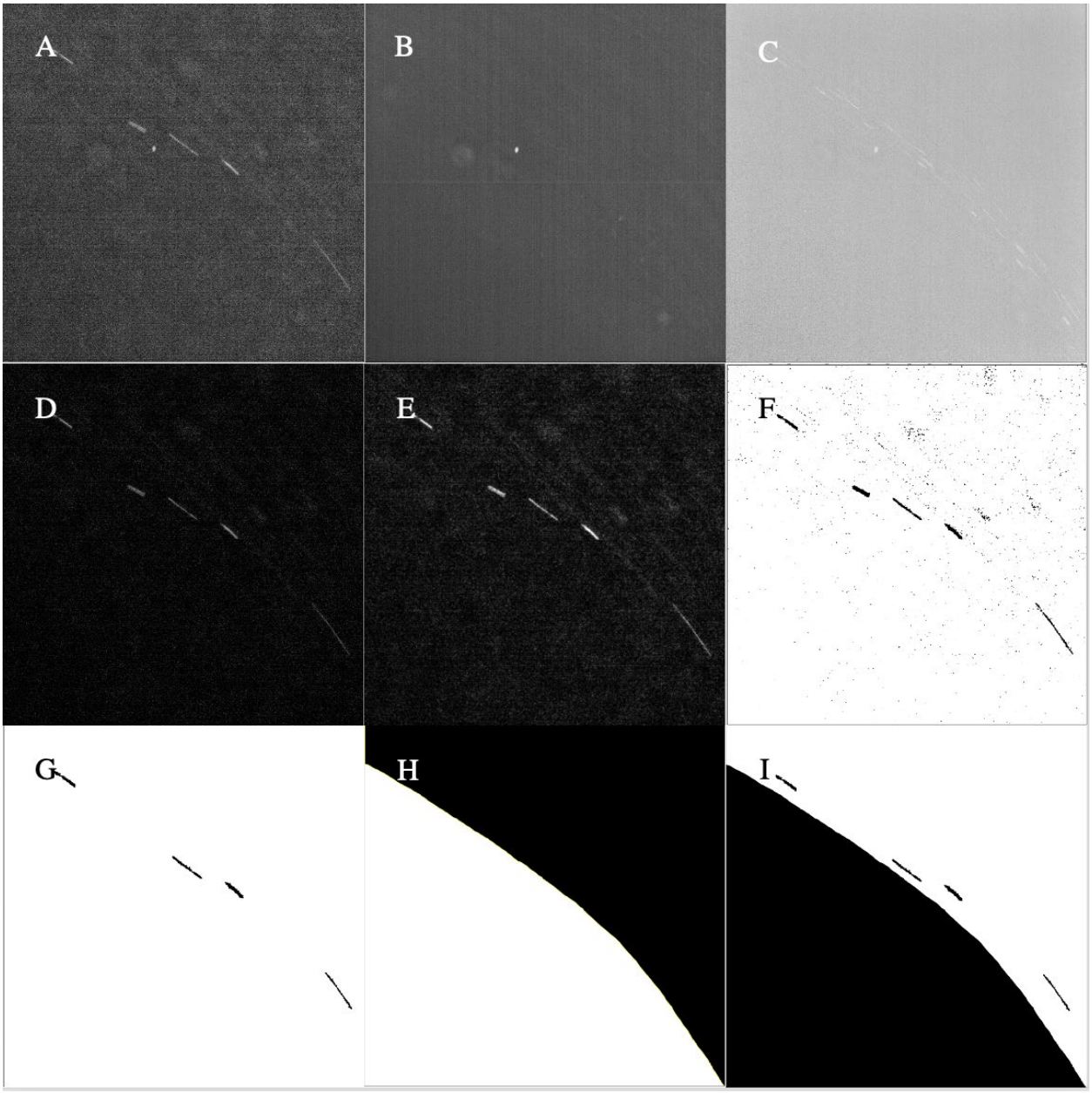

Figure 3: A) Raw data from bend inner wall region Patient 96 3 months at 300 mL/min. Image parameters: 40 ms exposure, 6.4X mag, 2 µm Invitrogen fluorescent beads, $3.5x10^{-6}$ % v/v bead concentration, and 6.3% (w/v) BMF. B) Average intensity projection of raw data. C) Maximum projection of raw data. D) The result of the raw data after the automated imaging step (auto enhancing contrast, subtract average Z projection, and despeckle) E) Brightness and contrast adjustment. F) Threshold adjustment G) Analyze particles command H) Manually selecting the wall outline from panel C using freehand select. Fill command on vein section, clear command on area outside. I) Final product before the Python imaging pipeline, panels G and H combined using the image calculator add.

Preliminary Results and Discussion

Optimization

We have previously created a model that was capable of measuring WSS in a patient specific way. However, it was only able to do so at physiologic blood flow rates, which is 15 - 44 mL/min, with experiments being conducted at 20 mL/min [42]. While the fluidic models were fabricated similar to the processes described in 'Materials and Methods', many changes were necessary to be made to the device fabrication and experimental procedure in order to attain increased flow rates in the fluidic models discussed in this study, consistent with blood flow rates measured in patient with AVF (referred to hereon as pathologic values). These changes successfully allowed our model to withstand flow rates up to and above 500 mL/min. At such high flow rates, image quality decreases and flow behavior becomes turbulent in some regions and cannot be processed for usable data using our current methods. This geometry specific laminar to turbulent flow shift will be elaborated upon later in this paper. Even though streamline data from turbulent flow cannot be used to calculate WSS, other useful data can still be understood, and the optimization changes made are an important step in using these models to improve patient care.

Changes in Device Fabrication

The millifluidic devices do not appear exactly as they did in our previous paper (Figure 3), because the fabrication procedure was changed[42]. Visually they have differences, but even more changes were made that are invisible in the final product. These changes resulted in clearer models with increased capabilities.

One invisible physical difference between these two versions of the models is in the mechanical stiffness of the fluidic devices. The previous version of the model used a ratio of 10

parts base to 1 part curing agent. The new models use 9 parts base to 1 part curing agent, making them slightly stiffer and able to withstand higher flow rates without deformation or breaking. 5 parts base to 1 part curing agent was attempted, but it created a version that set so quickly that air bubbles were trapped inside the model, distorting the patient specific geometry.

The model used in our previous study (Figure 4A), was also connected to the rest of the experimental set up via thinner tubing and had inlet and outlet cones to create a smooth transition between the patient vein and the smaller tubing. The thinner tubing (#6516T11, McMaster-Carr) had 1/16 inch inner diameter, while the new thicker tubing has 1/4 inch inner diameter (#5393K41, McMaster-Carr). Now that thicker tubing is being used, no inlet or outlet cones are needed (Figure 4C). This is because the diameters of the vein lumen and tubing are already similar, so no transition is needed. There are also no connector boxes. Previously the connector piece (#5117K52, McMaster-Carr) between the tubing and the fluidic model was encased in PDMS for stability. The current model uses connector pieces (#5117K61, McMaster-Carr) that are less prone to leaking, so the connector boxes are no longer necessary.

As the pressurized fluid reservoirs (Figure 2D) were not compatible with the tubing that connected to the models, leak-free tubing to tubing connections were required. The previous version of the tubing connections involved placing the smaller 1/32 inch PEEK tubing for the fluid reservoir inside the larger tubing and encasing the connection in resin (Figure 4B). It took much longer to make and was prone to leaks. Now the tubing-to-tubing connection use tubing connectors (#5117K61 McMaster-Carr) and caps compatible with 1/8 inch inner diameter tubing (#5238K718, McMaster-Carr) are used (Figure 4D). The smaller tubing used previously also caused pressure buildup in the models, making them swell, break the model, or increase the risk of leaks. The smaller tubing also limited the maximum possible flow rate.

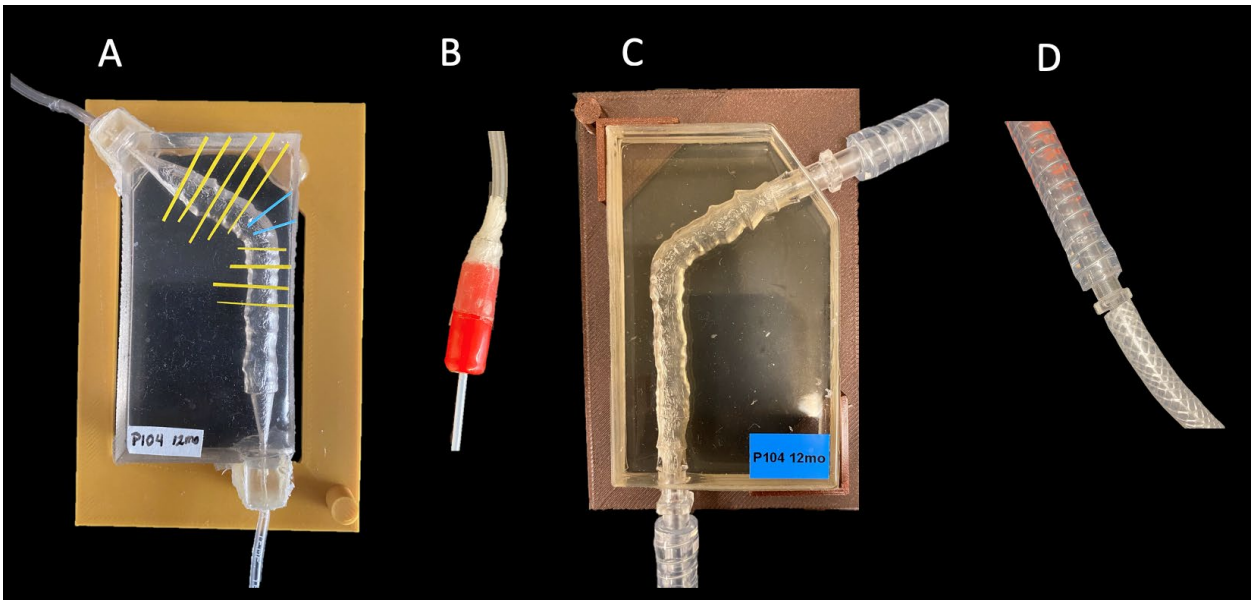

Figure 4: A) The version of the model for Patient 104, 12 months post AVF insertion, used in the previous paper[42]. This model has thin tubing, connector boxes, a flimsy PVA frame, is secured using hot glue, and inlet and outlet cones to merge the differing diameters of the patient vein and the tubing. B) The old version of the tubing connections. The two different tubings were connected by a plastic connector piece. This connection was covered by resin, which was poured into the red plastic mold. The red mold was covered by paraffin film to prevent the resin from leaking before it cured fully, which took 24 hours at room temperature. C) The current version of the model for Patient 104, 12 months post AVF insertion. The print has been flipped 180˚ for ease of use but does not differ in any other way. It has thicker tubing, no inlet/outlet cones, no connector boxes, and a better designed frame made of PLA. D) The new tubing connections used in the new version of the models. Connector pieces allow tubing from the model (top) to easily plug into the tubing connected to the fluid reservoirs (bottom). There are two of these connections on each model, one on the inlet tubing and one on the outlet tubing. This example is from the P104 12 months post AVF insertion inlet.

When the models are being autoclaved to dissolve the 3D print inside, the top and bottom of the devices are covered with aluminum foil. This prevents the model from discoloring due to the high heat and pressure and keeps them clearer which improves image quality.

Additionally, the frame that the model sits in when on the microscope stage is different. The previous frame was 3D printed using PVA. However, this frame was not very stiff and was

designed slightly too large for the microscope stage area, so it bent when in the stage. This caused some imaging difficulties as the frame occasionally obstructed the objective from being able to view the entire vein area. Additionally, the model was often tilted as a result, causing issues with the focus not being level across the vein. The new frames were also 3D printed using PLA and they are much stiffer than the previous frame version and were designed with the microscope stage's specifications. Now the models sit level on the microscope, resolving the earlier issues.

Some changes that were made do not affect the abilities of the model, but simply make it easier to use for experimentation. For convenience, the connecting tubing has also been redesigned so that models can easily be swapped in and out without disrupting the rest of the experimental setup. Now the majority of the tubing is permanently connected to the fluid reservoirs instead of permanently to the models. The thicker tubing from the models plugs into the slightly thinner fluid reservoir tubing, and can be unattached at the beginning and end of experimentation, as seen in Figure 3 D. Previously the tubing connections were permanent, seen in Figure 3 B. Other ease-of-use changes include rotating some of the prints 180˚ in orientation during fabrication and swapping the fluid reservoirs from 50 mL containers of BMF to 1 L bottles so that the fluid reservoirs do not need to be refilled as often during higher flow experiments.

Procedural Changes

Imaging parameters also had to be optimized for higher flow conditions. Table 1 shows the SNR results of the bead concentration and exposure time parameter sweep, where we tested 20 ms to 80 ms exposure times at 10 ms intervals for three bead concentrations. This value represents the image quality at each condition. Higher values correspond to better image quality. This allows optimization of conditions to be done in an unbiased quantitative method.

Exposure Time	20 ms	30 ms	40 ms	50 ms	60 ms	70 ms	80 ms
3.0 x 10^{-6} % v/v	7.05 ±0.07	7.52 ±0.09	8.20 ±0.07	8.60 ±0.04	8.71 ±0.05	9.19 ±0.05	9.06 ±0.01
3.5 x 10^{-6} % v/v	7.35 ± 0.06	7.87±0.09	8.14 ±0.02	8.42 ±0.02	9.05 ±0.02	8.98 ±0.05	8.88 ±0.02
4.0 x 10^{-6} % v/v	7.49 ±0.03	7.87 ±0.07	8.52 ±0.09	8.95 ±0.05	8.93 ±0.01	7.52 ±0.23	8.32 ±0.24

Table 1: SNR with standard deviation error for the optimization parameter sweep of bead concentration and exposure time. The optimal exposure time for each bead concentration is highlighted in green. SNR value shown is the mean of all SNR values in a 100 image stack at each condition. The SNR was calculated using an ImageJ plugin[49]. This plugin requires a comparison image for the SNR calculation. The comparison image used here was the tenth image in a stack taken in the inner wall bend region at 55 mL/min which was representative of quality data. Test images were taken at the inner wall on the prebend of Patient 98 3 months post AVF at 250 mL/min. Error for each condition calculated using the standard deviation command in Microsoft Excel.

From this data, image quality is best when 3.0 x 10^{-6} % v/v beads are used with 70 ms exposure time, with conditions 3.5 x 10^{-6} % v/v bead concentration at 60 ms exposure time and 4.0 x 10^{-6} % v/v bead concentration at 50 ms exposure time second and third best respectively. The standard deviation on these values is small, which makes these results significant. In our previous work at lower flow rates, we used 100 ms exposure time and 4.0 x 10^{-6} % v/v bead concentration. At higher flow rates, streamlines become longer and less distinct. Shortening the exposure time counteracts this effect by causing streamlines to be shorter, producing clearer data and better image quality. This parameter sweep was effective in testing ways to increase image quality at higher flow rates. However, even with this change in imaging parameters, there still exists more noise at higher flow rates than at lower flow rates. Decreasing the bead concentration decreases background noise, therefore increasing image quality.

However, the image quality data alone does not reveal which parameters are optimal. The highest SNR value implies that 3.0 x 10^{-6} % v/v bead concentration at 70 ms should provide the most optimal data. In reality, few data points are observed in these images due to the lower bead concentration. Because of this, the conditions at 3.5 x 10^{-6} % v/v beads and 60 ms were considered optimal during data collection at 250 mL/min to compromise between number of streamlines and data quality in order to optimize data collection. These imaging parameters are also flow rate dependent. Therefore, not all images were taken with these exact parameters depending on the flow rate for that experiment.

We also observed some inconsistencies when doing calibration curves for the pressure to flow rate relationship that prompted optimization fixes (Figure 5A). The R^2 for the line of best fit equation for P98 3mo was 0.93, below the significance threshold, and the line had several irregular humps. Additionally, when the same pressure was applied, sometimes there would be very different flow rate responses.

To understand why these inconsistencies were occurring, we aimed to make as many factors consistent as possible to rule out potential causes. As part of this aim, we standardized the inlet fluid reservoir so that the same bottle is used each time. We also adjusted the tubing to ensure no kinks occurred that could block and disrupt the flow. This was especially important in the tubing from the inlet fluid reservoir, as it is the smallest, most fragile, and most prone to bends and kinks. These difficulties with the calibration curves were not observed in the previous model versions that had only the smaller tubing, so we did a calibration curve with no model, only large tubing connected to the experimental set up to see if the issue was specific to the larger tubing. This curve still had the inconsistencies and was slower than the set up with the model. This was not logically consistent, as the curves should be identical or even faster as just the raw tubing without the model.

After refilling the fluid reservoir, the flow rates dramatically increased for the same pressure. This led to the discovery that the cap tightness on the fluid reservoirs has been responsible for the inconsistencies. The cap changed to accommodate the larger fluid reservoir but is also more difficult to close completely. With that new knowledge, the inconsistencies in the calibration curves were resolved. We marked each fluid reservoir change in orange on our calibration curves to confirm that the cap tightness was no longer influencing the results (Figure 5B). This led to the observation that similar to the previous humps in the calibration curve, there are trivial changes corresponding to the fluid reservoir changes even when the cap is completely closed. This is due to it being more difficult to maintain pressure in a larger space, which occurs in the fluid reservoir as the BMF is drained from the inlet bottle.

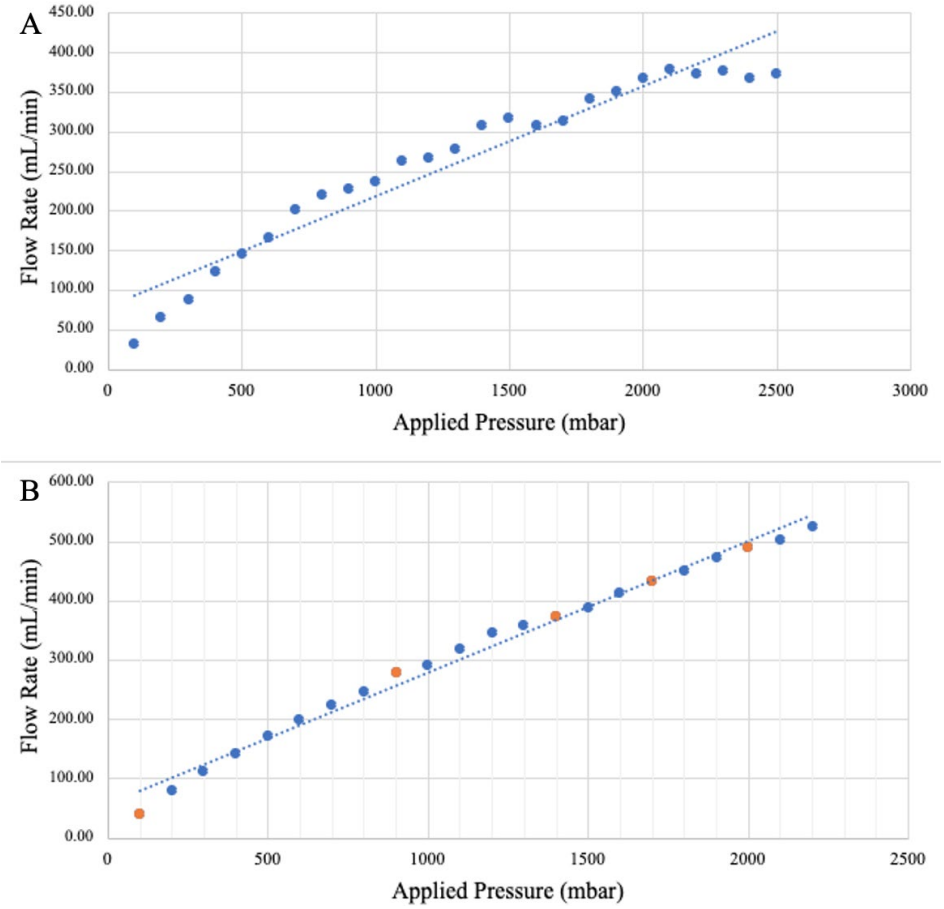

Figure 5: A) Calibration curve of the idealized model with 9mm diameter with inconsistencies. Equation for line of best fit, shown as a dotted blue line, is $y = 0.139x + 79.05$, while the R^2 is 0.93. There are several bumps in the line, with peaks around 800 mbar, 1100 mbar, 1500 mbar, 1800 mbar, and 2100 mbar. B) Calibration curve for idealized model with 9mm diameter after optimization to resolve inconsistencies. Every time the fluid reservoirs are refilled is marked in orange. Line of best fit for the calibration curve is $y = 0.2213x + 57.15$, and the R^2 is 0.99.

Calibration Curves

The results of the calibration curves for the models are shown below in Figure 6A. These calibration curves are necessary for running experiments, as the applied pressure to flow rate ratio is not the same for all fluidic devices. While the same pressure results in the same flow rate within a single model, the same pressure can result in very different flow rates between models. Because

experimentation is done with target flow rates, and not pressure, these calibration curves help standardize the applied flow rate during experiments.

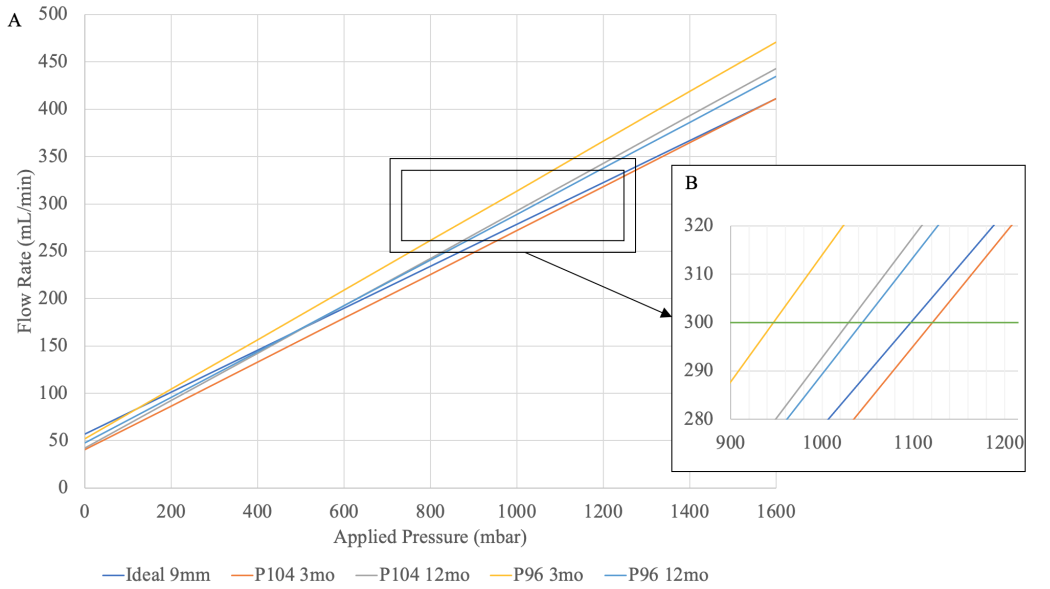

C

Model	Calibration Curve Equation	R^2	Vein Diameter	Applied Pressure at 300 mL/min
Ideal 9mm	Y = 0.2213X + 57.157	0.9881	9 mm	1097 mbar
P104 3mo	Y = 0.2315X + 40.49	0.9911	9 mm	1121 mbar
P104 12mo	Y = 0.2503X + 42.448	0.9874	11 mm	1029 mbar
P96 3mo	Y = 0.2617X + 52.19	0.9864	6.6 mm	947 mbar
P96 12mo	Y = 0.2418X + 47.533	0.9898	6.6 mm	1044 mbar

Figure 6: A) Graph showing the calibration curve lines for all models. The idealized model with diameter 9mm is shown in dark blue, Patient 104 3 months is orange, Patient 104 12 months is gray, Patient 96 3 months post AVF creation is yellow, and 12 months post AVF creation is light blue. The horizontal axis shows the applied pressure in mbar, which is the value input into the pressure regulator during calibration and experimentation. The flow rate is on the vertical axis in mL/min. This is the measured value of the amount of BMF in the output fluid reservoir over time. B) A close up around the value 300 mL/min, emphasized by the horizontal green line. The colors representing each model, as well as the horizontal and vertical axes are the same as in panel A. P96 3mo has the lowest applied pressure to reach 300 mL/min, with P104 12mo, P96 12mo, Ideal 9mm, and P104 3mo following respectively. C) Table showing the equations for the lines seen in panels A and B, the R^2 for the equations, the diameter of each model, and the numerical value for the applied pressure at 300 mL/min.

However, these calibration curves reveal more than just what pressure input to use during experiments. Due to the nature of how the flow rate is measured, by timing the increase of the fluid level in a graduated cylinder for the output flow, the calibration curves also act as a measure of

fluidic resistance. The applied pressure to flow rate relationship is influenced primarily by the diameter of the fluidic device. The equation representing this relationship is $Va = (\Delta P*D^4)/(128*\mu*L)$, where Va is flow rate, P is pressure, D is diameter, μ is viscosity, and L is the length of a straight pipe[50]. As the equation shows, for a given flow rate, if diameter increases, pressure needs to decrease in order to balance the equation. For the two time points for Patient 104, this is seen. Remodeling occurred over time, which increased the average diameter of the vein in the 12 month model compared to the 3 month model. As expected, the applied pressure necessary to reach 300 mL/min is lower for the 12 month model than the 3 month model.

That trend was not observed in Patient 96. While remodeling occurred between the two models, unlike in Patient 104, the average vein diameter stayed the same over time. However, the applied pressure necessary to reach 300 mL/min increased from the 3 month model to the 12 month model. This implied that though the average vein diameter remained the same, there is likely a small section in the 12 month model that is much thinner, creating a constraint on the flow. This corresponds to the observed patient outcome. Patient 96 has a stenosed region, where the vein remodels itself to become narrower, increasing the likelihood of thrombosis and raises the blood pressure. This explains why the applied pressure necessary for 300 mL/min is higher for the 12 month model than the 3 month model for Patient 96.

Comparing the applied pressure necessary to get to 300 mL/min in Figure 6 C for Patient 104 versus Patient 96 also gives an unexpected result. Based on their respective diameters, one would expect the applied pressure at 300 mL/min to be lower for both Patient 104 models than the Patient 96 models. Instead, the Patient 104 12 month model is only slightly lower than the Patient 96 12 month model, and is higher than the Patient 96-3 month model, even though it is nearly twice as large as either model for Patient 96. There is no clear explanation for this outcome. A

potential reason is the bend angle of the model influencing how easily flow passes through the model, because the Patient 104 models have a much sharper bend than the Patient 96 models.

Image Quality

The image quality for the preliminary data was quantified using their SNR compared to a reference image, shown in Table 2. Here we are able to compare the SNR values for all models, including the idealized model. The SNR values for all of the patient models were relatively similar, while the idealized model has higher SNR values for all ROIs.

SNR Table for all Models					
ROI	Ideal 9mm	P104 3mo	P104 12mo	P96 3mo	P96 12mo
Prebend Inner Wall	8.41 ± 0.03	6.15 ± 0.01	6.26 ± 0.02	6.18 ± 0.01	6.14 ± 0.01
Prebend Outer Wall	9.65 ± 0.09	6.18 ± 0.01	6.29 ± 0.02	6.18 ± 0.01	6.13 ± 0.01
Bend Inner Wall	7.85 ± 0.24	6.21 ± 0.01	6.23 ± 0.02	6.20 ± 0.01	6.20 ± 0.01
Bend Outer Wall	9.01 ± 0.08	6.17 ± 0.01	6.16 ± 0.01	6.16 ± 0.01	6.64 ± 0.01
Postbend Inner Wall	8.30 ± 0.03	6.19 ± 0.01	6.27 ± 0.02	6.19 ± 0.01	6.17 ± 0.01
Postbend Outer Wall	8.80 ± 0.16	6.14 ± 0.01	6.19 ± 0.01	6.16 ± 0.01	6.22 ± 0.01

Table 2: SNR Table for all four patient models and the idealized model at 300 mL/min. The SNR values are separated into six regions of interest; prebend, bend, and postbend inner and outer walls. The SNR values are shown, as well as the standard deviation for each ROI. The SNR values were calculated using an ImageJ plugin[49]. The reference image used for the SNR calculation was the tenth image in a stack taken in the inner wall bend region of Patient 98 3 month model at 55 mL/min and 70 ms exposure time which was representative of quality data. The error for each condition was calculated using the standard deviation command in Microsoft Excel.

The idealized 9 mm model has the most variation in its SNR values. This is unexpected, because one would assume that the smooth idealized model should be very similar between ROIs. There is not a clear explanation for the phenomenon. It is likely that the smooth walls of the idealized model are not as smooth as was intended, retaining the variation from the 3D print used to create the model, and this is responsible for the variation in SNR values. If this is the cause, the most interference from the print would occur in the bend inner wall region, as the SNR is lowest in this ROI. The walls of the idealized model are still smoother than those of the patient models, explaining why the SNR is higher for all ROIs in the idealized model; there is less background noise from the patient specific geometry.

When the SNR values in Table 2 are compared to those from Table 1 for parameter optimization from earlier, these values are lower. This is expected, as these values were calculated from experiments run at 300 mL/min instead of 250 mL/min. The increase in flow rate creates more background noise, which lowers the SNR values.

Wall Shear Stress

Table 3 compares the average WSS value of each major region of the Idealized 9mm diameter model and all Patient 104 and Patient 96 models. The numbers in the table are the average WSS value of all streamlines from the image-stack of the given ROI. To understand the impact of high flow, the experiments were run at 300 mL/min.

In the idealized pathologic 9 mm diameter model, the bend outer wall and the postbend outer wall both have lower WSS than the rest of the model. If the connection between low WSS and risk of thrombosis is accurate, then these areas are at higher risk. The prebend region has the highest WSS because the velocity of the flow is highest in that region. The introduction of the turn in the bend which creates more complex flow results in slower flow near the wall and therefore lower WSS. Because this model is the smooth idealized model, the results here are purely due to the bend as there is no other specific geometry. The bend is likely the reason that the cephalic arch is at such high risk for complications, which is supported by the results of this WSS profile.

In the Patient 104 models, there is change between the two timepoints. The prebend inner, as well as both postbend regions, are much lower in the 12 month model than in the 3 month model. From this, one can conclude that Patient 104's risk of dialysis complications increased over time, and that the postbend may be a particularly vulnerable region. Additionally, the bend inner wall region of the 12 month model does not have a WSS value. This is because this region had turbulent

flow. Turbulent flow is when the flow behavior is very chaotic. Instead of clearly defined streamlines, the data collection produces fuzzy, indistinct, swirly lines that cannot be processed for WSS data. Even though WSS cannot be calculated here, turbulent flow is also damaging to the endothelium, so the bend inner region can be added to the list of areas at risk in this model. The bend inner wall region of this model is also designated most at risk in the computational study[41]. This data implies that Patient 104 is now more at risk for complications as time passes.

Unlike in Patient 104, Patient 96 has several regions where WSS increases. Specifically the outer wall of the prebend and the inner wall of the bend both increase. High shear stress is beneficial for endothelial cells. One explanation for this is vein remodeling over time to improve the flow conditions. However, in every other region in Patient 96 the WSS value decreased. This includes the prebend inner wall, the bend outer wall, and both postbend regions. These regions are therefore at higher risk for complications. Because more regions have much lower WSS in the 12 month model than regions that have higher WSS, the 12 month model is overall more at risk for complications. Patient 96, like Patient 104, has become more at risk for complications over time.

ROI	Idealized 9mm	P104 3mo	P104 12mo	P96 3mo	P96 12mo
Prebend Inner	218.66 ± 40.03	383.23 ± 173.14	51.6 ± 13.02	328.64 ± 161.63	131.66 ± 56.54
Prebend Outer	137.11 ± 54.45	186.41 ± 61.12	137.22 ± 60.45	230.36 ± 76.64	352.42 ± 180.15
Bend Inner	77.72 ± 21.69	134.48 ± 33.56	- -	218.61 ± 69.61	547.51 ± 212.5
Bend Outer	145.05 ± 197.07	139.18 ± 58.44	135.11 ± 48.64	227.97 ± 70.59	181.5 ± 83.57
Postbend Inner	73.17 ± 9.98	209.23 ± 132.57	62.77 ± 11.61	426.05 ± 485.26	151.81 ± 64.16
Postbend Outer	189.76 ± 91.73	272.24 ± 168.72	69.92 ± 32.95	137.21 ± 50.44	76.9 ± 20.33

Table 3: Wall Shear Stress global mean values with the standard deviation shown in mPa. Values are shown for the Prebend Inner and Outer wall regions, the Bend Inner and Outer wall regions, and the Postbend Inner and Outer regions for a total of six ROIs per model. The Idealized 9mm model, both Patient 104 models, and both Patient 96 models are shown. This data is the result of the image processing Python pipeline that generates WSS profiles. The value for the inner wall of the bend region for the Patient 104 12 months post AVF installation model is missing because it could not be processed due to turbulence.

These results are contrasted by the models at physiologic flow at 20 mL/min from the previous study in Table 4[42]. At physiologic flow rates, the models produce WSS values below the typical range of 76 - 760 mPa[27,42]. This is expected, because these veins are not physiologic healthy veins and would never experience this flow rate in the body. In contrast, a model that matches the size of healthy physiologic veins, the idealized 3 mm diameter model, generates WSS values within this range at physiologic flow rates. The typical blood flow range during dialysis is 300-500 mL/min according to DaVita, one of the largest dialysis providers in the US[51]. When the patient models experience flow rates within the dialysis range, the global WSS mean values are now within the physiologic range for veins. This provides support for the validity of the models, that only flow rates that would occur in a dialysis patient produced normal WSS values with the

dialysis models, while a physiologic model can produce those same WSS values at physiologic flow rates.

Model	20 mL/min (mPa)	300 mL/min (mPa)
Idealized 3mm	255.38 ± 54.08	- -
P104 3mo	35.75 ± 3.91	220.795 ± 94.3
P104 12mo	26.89 ± 6.18	91.324 ± 41.46
P96 3mo	54.11 ± 10.32	261.47 ± 100.96
P96 12mo	70.76 ± 3.26	240.3 ± 177.05

Table 4: WSS global mean values for the entire model shown in mPa. Values for the 20 mL/min are taken from the paper "Creating patient-specific vein models to characterize wall shear stress in hemodialysis population" by Moya Rodriguez 2022[42]. The 300 mL/min data is the average of the data shown in Table 3, calculated using the AVERAGE and STDEV commands in Microsoft Excel.

Flow Sweep

As flow increased, streamlines generally became longer, corresponding to their increased velocity. Most of the flow stayed laminar (Figure 7). However, occasionally they exhibited more complex behavior as the flow rates changed. This ranged from flow perpendicular instead of parallel to the wall (Figure 8), recirculation pools (Figure 9), to turbulence (Figure 10). Because of image quality degradation at high flow rates during turbulence, WSS could not be calculated at turbulent flow, so this data is purely qualitative. These flow sweeps were conducted by systematically increasing the applied pressure by 100 mbar from 100 mbar up to 1500 mbar at 4X

magnification. The corresponding flow rate values are shown with the applied pressures across flow sweeps (Figures 6-9).

The most common flow behavior seen was laminar flow. Most regions remained laminar far past when other regions transitioned in non-laminar flow. For example, in Figure 7, unlike Figures 8-10, flow stays laminar up to 1500 mbar. Figure 7 depicts the prebend region in the Patient 104 3 month model. This difference in behavior is likely due to the vein geometry of each region, because areas with smooth straight walls were more likely to remain laminar, while areas with roughness or curve were more likely to develop complex flow behavior.

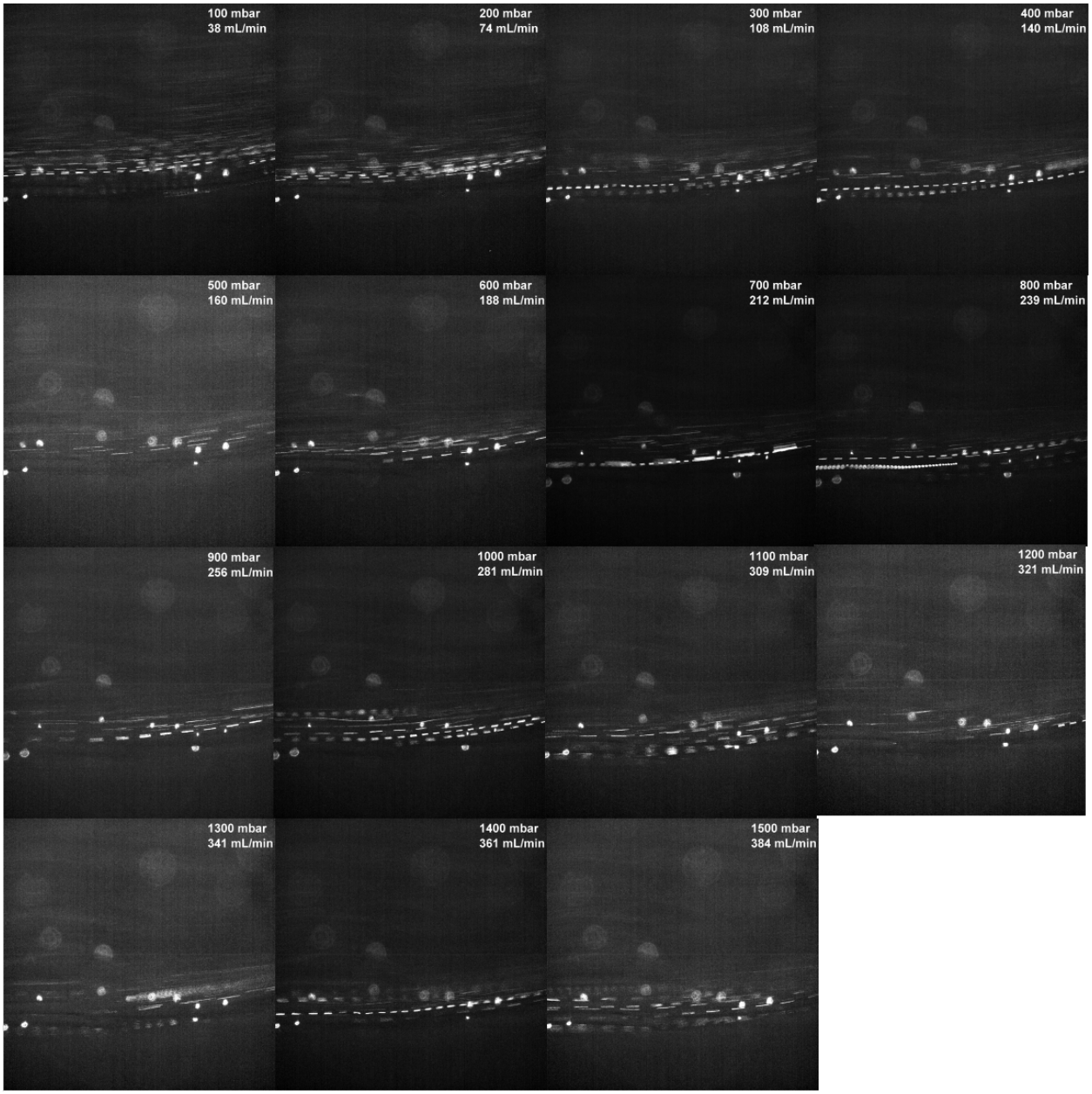

Figure 7: Laminar flow sweep from 100 mbar to 1500 mbar for the prebend inner wall region of Patient 104 3 months post AVF installation model. The flow stays laminar throughout the flow sweep. Pressure input and corresponding flow rate is shown in white in the top right corner of each image. Each image is the maximum intensity Z projection created from 50 images at each condition, created using ImageJ.

One example of complex flow behavior observed was the transition of streamlines from parallel to perpendicular with respect to the wall. Figure 8 illustrates how the flow behavior is a

function of the flow rate. As the flow rate increases, the angle of the streamlines to the wall, with the flow approaching perpendicularity to the wall at higher flow rates. This behavior begins around 500 mbar, or 160 mL/min, where it can be seen that the flow no longer resembles the images before it. From 100 - 400 mbar, or 38-140 mL/min, the flow is laminar and parallel to the vein wall. As quickly as 600 mbar, or 188 mL/min, the flow appears completely perpendicular to the wall. This continues for the remainder of the flow sweep, all the way until 1500 mbar, or 384 mL/min. As the flow rate increases from this point, the flow behavior becomes more chaotic but does not change shape. This is occurring in the inner wall of the postbend region in the Patient 104 3 months model. Specifically, this is situated where the flow rebounds from after hitting the curve in the bend region, which explains why the flow becomes perpendicular as the flow rates increase. At higher flow rates, instead of gently following the curve of the vein, the flow bounces off of the curve because of its increased speed and force. This type of complex flow will therefore be greatly impacted by the vein geometry and bend angle. Patients with a sharper bend in the cephalic arch will be more likely to see this type of flow, while patients with a smoother bend are less likely. This complex flow type was seen in this region in both of the Patient 104 models, which both have strong bend angles. This flow will be strongly hitting the endothelium at this location, potentially damaging and inflaming it, which can increase the risk for thrombosis and stenosis. This is an example of how patient specific geometry can impact patient outcomes and could be a useful addition to a clinician's toolkit when designing treatment.

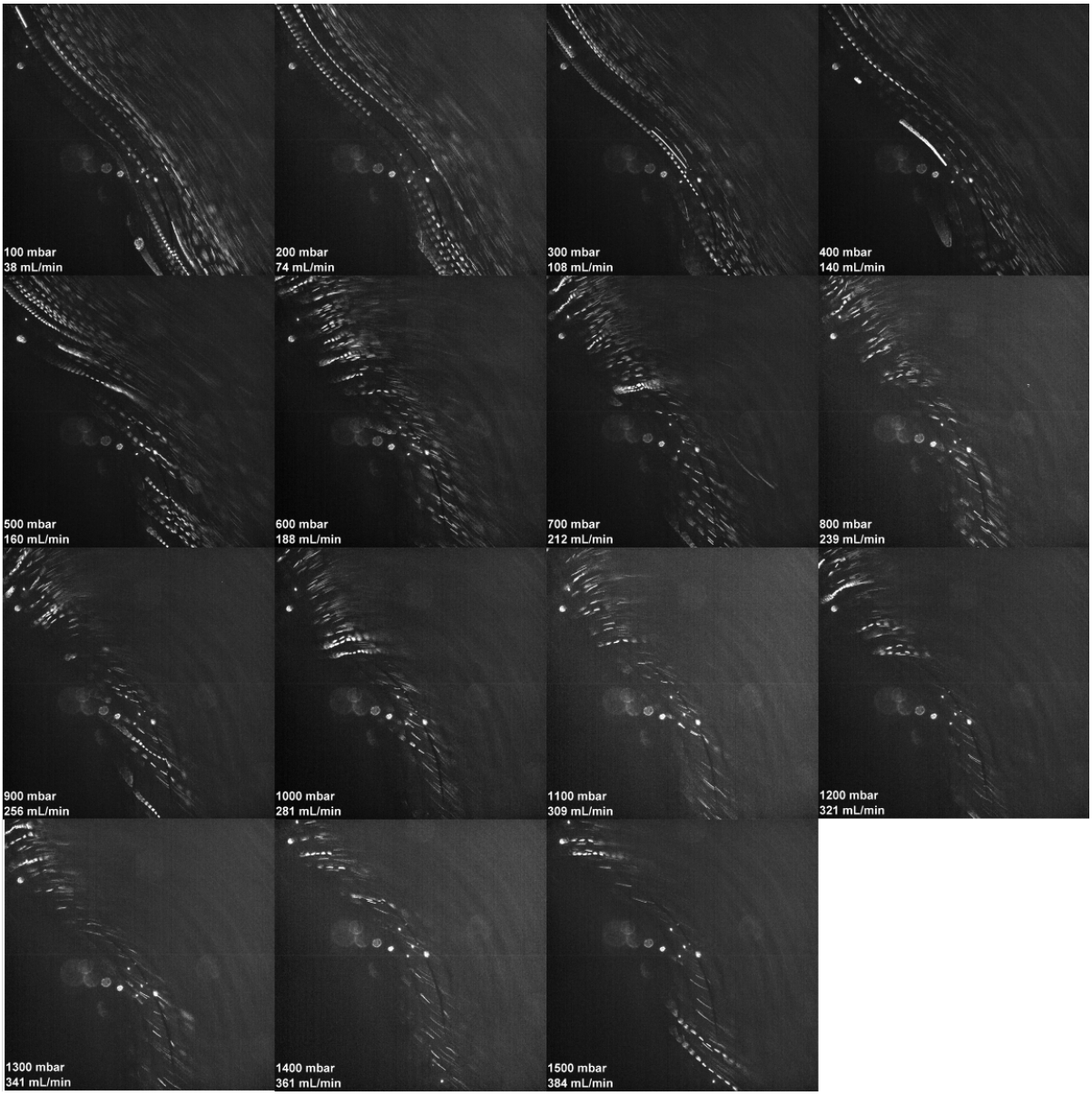

Figure 8: Flow sweep of the postbend inner wall region of the Patient 104 3 months post AVF installation model. Sweep goes from 100 mbar to 1500 mbar with every 100 mbar being shown at 4X magnification. The images seen are the maximum intensity Z projections from an image stack of 50 images at each condition, which was processed using ImageJ. The flow transitions from laminar and parallel to the wall, to complex and perpendicular to the wall, beginning around 600 mbar. The pressure input and corresponding flow rates are shown in white in the bottom left corner of the images.

Another form of complex behavior seen was a recirculation pool. A recirculation pool is where the flow travels in a circular motion in a particular region. In Figure 9, flow goes from laminar to a recirculation pool in the inner wall of the bend region of the Patient 104 3 months post AVF installation model as flow rates increase. The flow stops being laminar very early, at 300 mbar or 108 mL/min. It is a full recirculation pool by 500 mbar, or 160 mL/min. That is at lower flow rates than dialysis treatment runs at or the typical flow rate in a fistula[51]. Recirculation pools may concentrate pro-thrombotic factors and increase the risk of thrombosis in a region.

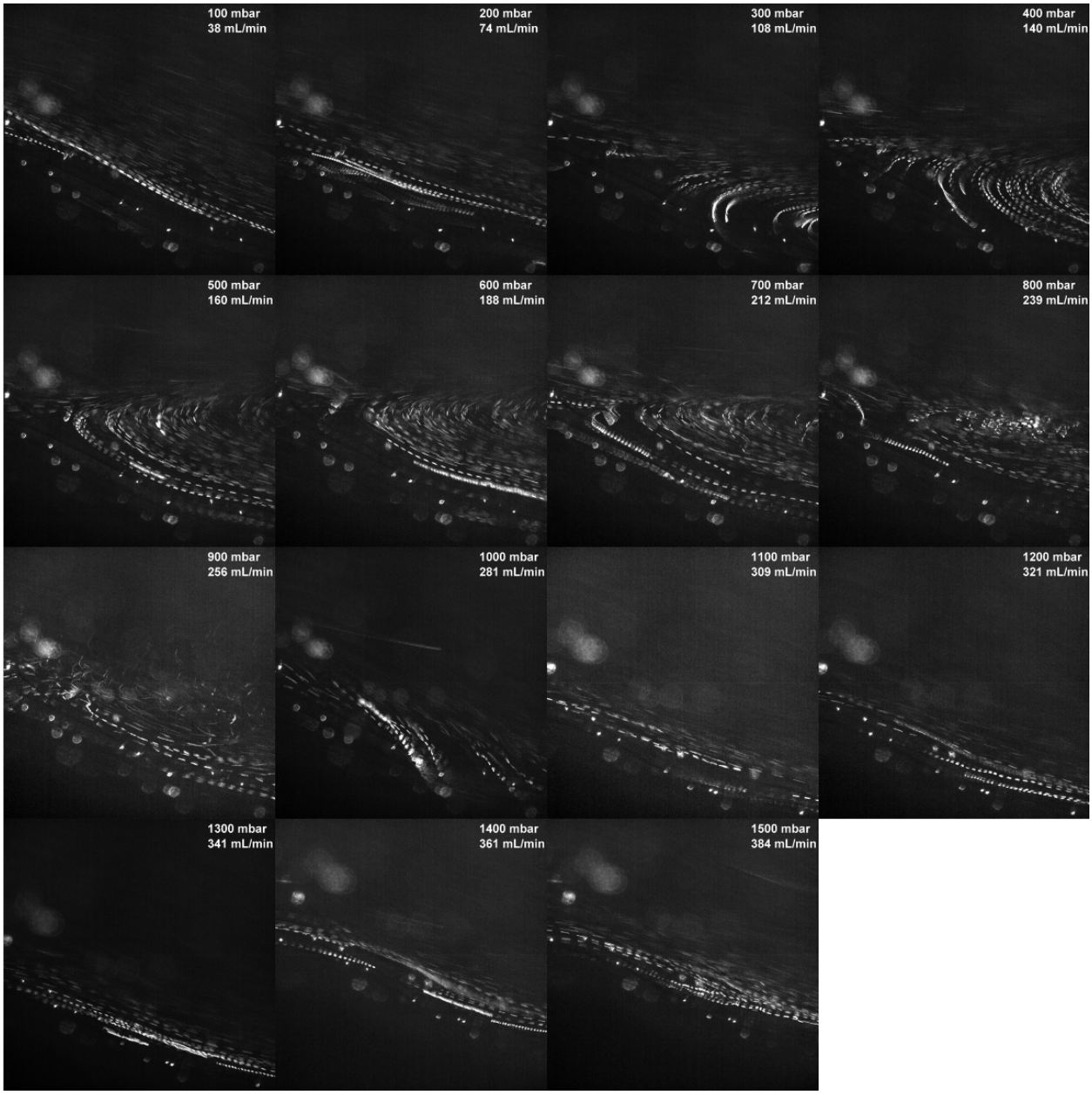

Figure 9: Flow sweep of the bend inner wall region of the Patient 104 3 months post AVF installation model. Sweep goes from 100 mbar to 1500 mbar with every 100 mbar being shown. The images seen are the maximum intensity Z projections from an image stack of 50 images at each condition, which was processed using ImageJ. The flow transitions from laminar, to a recirculation pool starting at 300 mbar, back to laminar to 1100 mbar. The pressure input and corresponding flow rates are shown in white in the top right corner of the images.

Most of the time, complex flow does not return to laminar flow. However, an example where that does occur can be seen in Figure 9. The complex flow moves into the postbend region

as the flow rates increase and leaves the bend inner region shown. These images are the only time we observed the center of a recirculation pool move positions in our models, but introduces the idea that complex flow is a function of both the flow rate and the vein geometry. Previously, we assumed that the type of complex flow was purely a result of the vein geometry. However things are rarely so simple, and this ROI is a good example of how the flow characteristics are the result of a complex interplay between the vein and flow.

Turbulent flow was also seen in the postbend inner wall of Patient 104 3 months in Figure 10. It is difficult to analyze turbulent flow, because the streamlines are very different from how they appear during other types of flow. Instead of being straight clear lines, they are often curved and partially indistinct from rapidly entering and leaving the plane of focus. Additionally, there is often no overarching structure to the flow that allows broad analysis of behavior as flow rates increase.

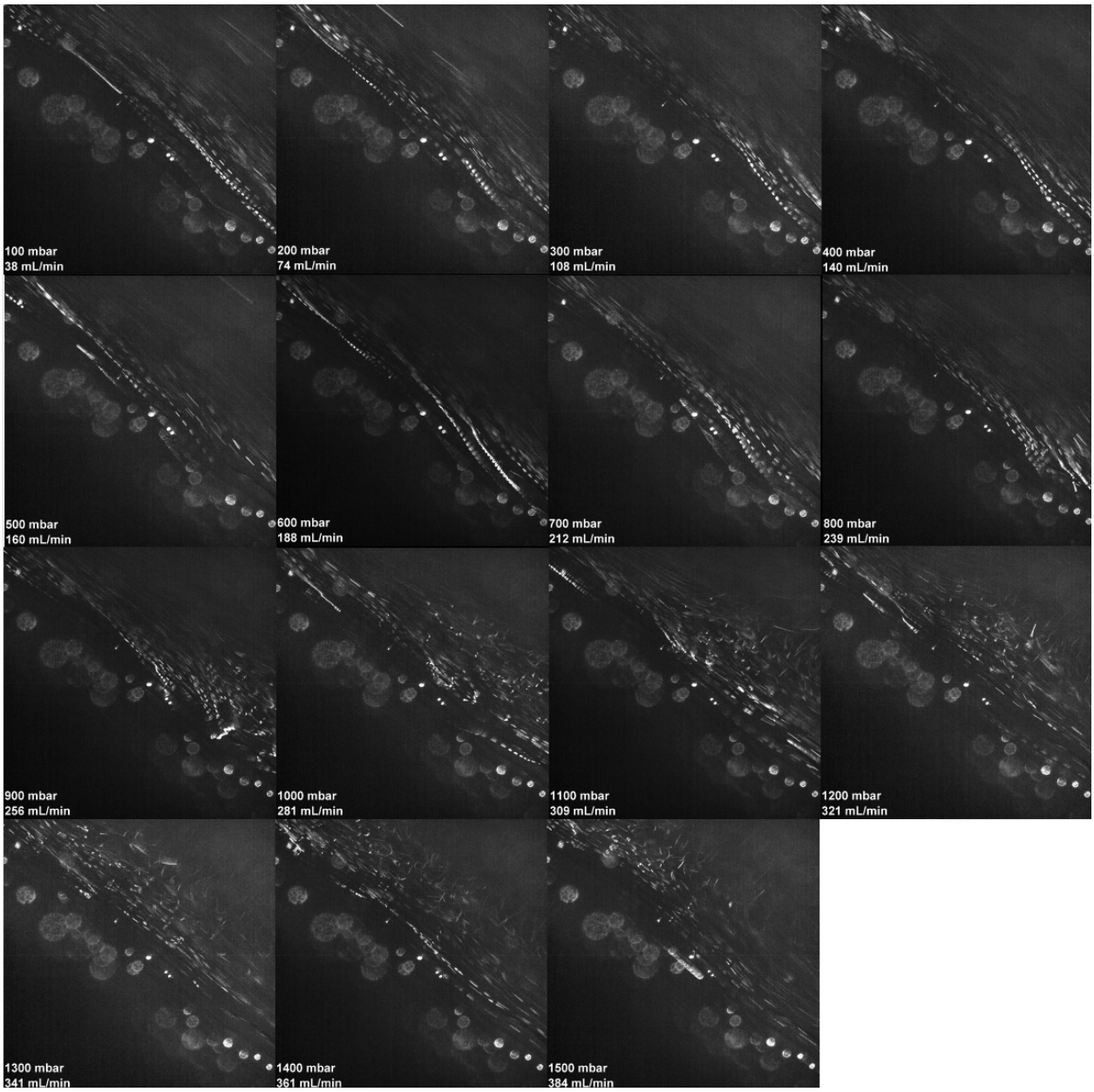

Figure 10: Turbulent flow sweep in the postbend inner wall region of the Patient 104 3 month model. Pressure and flow rate are shown in the bottom left. Maximum projections of 50 images at each condition from 100 to 1500 mbar in increments of 100 mbar. Laminar flow behavior from 100 to 800 mbar. Turbulent flow conditions seen at 900 mbar and higher.

These Figures 6-9 reinforce the importance of vein geometry and flow rates on flow. Each region exhibits different behavior at the same flow rates. These differences likely lead to some areas being higher risk for complication due to flow characteristics. Understanding where in the

vein is at risk and why may allow early intervention for dialysis complications or complete prevention in a patient specific manner.

Conclusions

Vein models replicating dialysis patient veins can reveal patient specific responses to different flow rates. This was done by generating WSS profiles and doing flow sweeps of the models. The WSS profiles showed regions of low WSS, which has been linked to poor patient outcomes and dialysis complications. Something surprising was observed during the flow sweep from low to high flow. Complex flow, which may also be linked to low WSS and dialysis complications, was seen at much lower flow rates than expected. Recirculation pools began appearing at values as low as 300 mbar or 108 mL/min, while laminar flow was consistently observed at physiologic (15-44 mL/min) flow rates. This is below the typical blood flow rate that dialysis treatment occurs at, between 300-500 mL/min, and below the normal blood flow rate in fistulas, which is as high as 600 mL/min[51,52]. This indicates that complex flow is occurring in these veins during both treatment and daily life. If complex flow is associated with damage to the endothelium and increased risk of stenosis and thrombosis, then lower flow rates than expected are still damaging to the patient. Keeping dialysis treatment below this flow rate value could maintain laminar flow and benefit the vein wall health and reduce the risk of dialysis complications in a patient specific manner, as complex flow begins at different flow rates depending on the vein geometry. This could explain why Japan, where the average blood flow rate during dialysis is 200 mL/min, has consistently fewer dialysis complications and fewer fistula failures[7,53–55]. Complex flow could also interfere with endothelial cell growth, as proper WSS is an important factor in establishing cell polarity, growth, and function.

Future directions

In the future we would like to finish characterizing laminar to complex flow and the patient specific geometries that contribute to this transition. Additionally, we would like to develop the ability to process turbulent and complex flow for WSS values, potentially using machine learning or a faster camera that can image with very short exposure times. This would allow us to compare degrees of turbulence and compare turbulent flow to laminar flow. To make the models more physiologically accurate, pulsatile flow would ideally be added to the models. This has been previously attempted and failed due to difficulties when processing to match the oscillation of the pulse to the data and difficulty establishing if the models were experiencing pulsatile flow or merely the average flow rate.

The next major desired change to the models is seeding them with endothelial cells to observe how the endothelium responds to WSS and flow. This brings along a new set of challenges to overcome. Ideally, the cells would undergo RNA sequencing after experiencing flow to identify how the cells responded to different WSS values, low versus high flow rates, or laminar versus complex flow behavior. Blood could be added to these models to observe the biochemical factors behind thrombosis and stenosis, not just the biophysical. However, experiments would require a large amount of blood to be feasible, which creates logistical complications. Ideally, the patient's own blood would be used in their vein models to make it as physiologically relevant as possible.

Anecdotally we observed less turbulence in the Patient 104 12 month model compared to the 3 month time point. This is potentially the result of the vein remodeling over time to reduce the amount of turbulence in the vein, however there is not currently enough data to make any conclusive statements. This is an interesting path we may follow in the future, to see if the vein

always remodels over time to minimize the amount of turbulence or complex flow in the vein and what factors contribute to this remodeling.

Works Cited

(1) *Annual Data Report*. USRDS. https://adr.usrds.org/ (accessed 2023-04-13).
(2) Glorieux, G.; Tattersall, J. Uraemic Toxins and New Methods to Control Their Accumulation: Game Changers for the Concept of Dialysis Adequacy. *Clin. Kidney J.* **2015**, *8* (4), 353–362. https://doi.org/10.1093/ckj/sfv034.
(3) Magnani, S.; Atti, M. Uremic Toxins and Blood Purification: A Review of Current Evidence and Future Perspectives. *Toxins* **2021**, *13* (4), 246. https://doi.org/10.3390/toxins13040246.
(4) Vanholder, R.; Van Laecke, S.; Glorieux, G. What Is New in Uremic Toxicity? *Pediatr. Nephrol. Berl. Ger.* **2008**, *23* (8), 1211–1221. https://doi.org/10.1007/s00467-008-0762-9.
(5) Vanholder, R.; Glorieux, G.; De Smet, R.; Lameire, N.; European Uremic Toxin Work Group. New Insights in Uremic Toxins. *Kidney Int. Suppl.* **2003**, No. 84, S6-10. https://doi.org/10.1046/j.1523-1755.63.s84.43.x.
(6) Chmielewski, M.; Cohen, G.; Wiecek, A.; Jesús Carrero, J. The Peptidic Middle Molecules: Is Molecular Weight Doing the Trick? *Semin. Nephrol.* **2014**, *34* (2), 118–134. https://doi.org/10.1016/j.semnephrol.2014.02.005.
(7) Pisoni, R. L.; Zepel, L.; Fluck, R.; Lok, C. E.; Kawanishi, H.; Süleymanlar, G.; Wasse, H.; Tentori, F.; Zee, J.; Li, Y.; Schaubel, D.; Burke, S.; Robinson, B. International Differences in the Location and Use of Arteriovenous Accesses Created for Hemodialysis: Results From the Dialysis Outcomes and Practice Patterns Study (DOPPS). *Am. J. Kidney Dis.* **2018**, *71* (4), 469–478. https://doi.org/10.1053/j.ajkd.2017.09.012.
(8) *Thrombosis in End-Stage Renal Disease - Casserly - 2003 - Seminars in Dialysis - Wiley Online Library*. https://onlinelibrary.wiley.com/doi/full/10.1046/j.1525-139X.2003.16048.x (accessed 2023-02-01).
(9) MacRae, J. M.; Dipchand, C.; Oliver, M.; Moist, L.; Lok, C.; Clark, E.; Hiremath, S.; Kappel, J.; Kiaii, M.; Luscombe, R.; Miller, L. M. Arteriovenous Access Failure, Stenosis, and Thrombosis. *Can. J. Kidney Health Dis.* **2016**, *3*, 2054358116669126. https://doi.org/10.1177/2054358116669126.
(10) Russo, T. A.; Stoll, D.; Nader, H. B.; Dreyfuss, J. L. Mechanical Stretch Implications for Vascular Endothelial Cells: Altered Extracellular Matrix Synthesis and Remodeling in Pathological Conditions. *Life Sci.* **2018**, *213*, 214–225. https://doi.org/10.1016/j.lfs.2018.10.030.
(11) Park, K. A.; Jo, H. M.; Han, J. S.; Kim, M. J.; Kwun, D. H.; Park, M. Y.; Choi, S. J.; Kim, J. K.; Hwang, S. D. Features of Atherosclerosis in Hemodialysis Patients. *Kidney Res. Clin. Pract.* **2013**, *32* (4), 177–182. https://doi.org/10.1016/j.krcp.2013.10.002.
(12) Jia, L.; Wang, L.; Wei, F.; Yu, H.; Dong, H.; Wang, B.; Lu, Z.; Sun, G.; Chen, H.; Meng, J.; Li, B.; Zhang, R.; Bi, X.; Wang, Z.; Pang, H.; Jiang, A. Effects of Wall Shear Stress in Venous Neointimal Hyperplasia of Arteriovenous Fistulae. *Nephrology* **2015**, *20* (5), 335–342. https://doi.org/10.1111/nep.12394.
(13) *Medicare Costs Associated With Arteriovenous Fistulas Among US Hemodialysis Patients - ScienceDirect*. https://www.sciencedirect.com/science/article/pii/S0272638618301240?via%3Dihub (accessed 2023-02-01).
(14) Delanaye, P.; Mariat, C.; Glassock, R. J. Safety of Living Kidney Donation:

Another Brick in the Wall…and a Solid (Physiologic) One. *Am. J. Kidney Dis. Off. J. Natl. Kidney Found.* **2015**, *66* (1), 1–3. https://doi.org/10.1053/j.ajkd.2015.04.005.
(15) Dolmatch, B.; Hogan, A.; Ferko, N. An Economic Analysis of Stent Grafts for Treatment of Vascular Access Stenosis: Point-of-Care and Medicare Perspectives in the United States. *J. Vasc. Interv. Radiol.* **2018**, *29* (6), 765-773.e2. https://doi.org/10.1016/j.jvir.2018.01.777.
(16) Quencer, K. B.; Oklu, R. Hemodialysis Access Thrombosis. *Cardiovasc. Diagn. Ther.* **2017**, *7* (Suppl 3), S299–S308. https://doi.org/10.21037/cdt.2017.09.08.
(17) Hammes, M.; Funaki, B.; Coe, F. L. Cephalic Arch Stenosis in Patients with Fistula Access for Hemodialysis: Relationship to Diabetes and Thrombosis. *Hemodial. Int. Int. Symp. Home Hemodial.* **2008**, *12* (1), 85–89. https://doi.org/10.1111/j.1542-4758.2008.00246.x.
(18) Elamurugan, E.; Hemachandar, R. Brachiocephalic Arteriovenous Fistula for Hemodialysis through the Median Antecubital Vein. *Indian J. Nephrol.* **2017**, *27* (3), 177–180. https://doi.org/10.4103/0971-4065.179333.
(19) Hammes, M.; Boghosian, M.; Cassel, K.; Watson, S.; Funaki, B.; Doshi, T.; Akherat, S. M. J. M.; Hines, J.; Coe, F. Increased Inlet Blood Flow Velocity Predicts Low Wall Shear Stress in the Cephalic Arch of Patients with Brachiocephalic Fistula Access. *PLOS ONE* **2016**, *11* (4), e0152873. https://doi.org/10.1371/journal.pone.0152873.
(20) *Clinical predictors of recurrent cephalic arch stenosis and impact of the access flow reduction on the patency rate - Yaeni Kim, Hyung Duk Kim, Byung Ha Chung, Cheol Whee Park, Chul Woo Yang, Yong-Soo Kim, 2022*. https://journals.sagepub.com/doi/10.1177/11297298211008758 (accessed 2023-02-01).
(21) Zhang, J. X. J.; Hoshino, K. Chapter 3 - Microfluidics and Micro Total Analytical Systems. In *Molecular Sensors and Nanodevices*; Zhang, J. X. J., Hoshino, K., Eds.; William Andrew Publishing: Oxford, 2014; pp 103–168. https://doi.org/10.1016/B978-1-4557-7631-3.00003-X.
(22) Millon, A.; Sigovan, M.; Boussel, L.; Mathevet, J.-L.; Louzier, V.; Paquet, C.; Geloen, A.; Provost, N.; Majd, Z.; Patsouris, D.; Serusclat, A.; Canet-Soulas, E. Low WSS Induces Intimal Thickening, While Large WSS Variation and Inflammation Induce Medial Thinning, in an Animal Model of Atherosclerosis. *PLOS ONE* **2015**, *10* (11), e0141880. https://doi.org/10.1371/journal.pone.0141880.
(23) Remuzzi, A.; Bozzetto, M.; Brambilla, P. Is Shear Stress the Key Factor for AVF Maturation? *J. Vasc. Access* **2017**, *18* (1_suppl), S10–S14. https://doi.org/10.5301/jva.5000686.
(24) Browne, L. D.; Bashar, K.; Griffin, P.; Kavanagh, E. G.; Walsh, S. R.; Walsh, M. T. The Role of Shear Stress in Arteriovenous Fistula Maturation and Failure: A Systematic Review. *PLOS ONE* **2015**, *10* (12), e0145795. https://doi.org/10.1371/journal.pone.0145795.
(25) Davies, P. F. Hemodynamic Shear Stress and the Endothelium in Cardiovascular Pathophysiology. *Nat. Clin. Pract. Cardiovasc. Med.* **2009**, *6* (1), 16–26. https://doi.org/10.1038/ncpcardio1397.
(26) Reneman, R. S.; Arts, T.; Hoeks, A. P. G. Wall Shear Stress – an Important Determinant of Endothelial Cell Function and Structure – in the Arterial System in Vivo. *J. Vasc. Res.* **2006**, *43* (3), 251–269. https://doi.org/10.1159/000091648.
(27) Malek, A. M.; Alper, S. L.; Izumo, S. Hemodynamic Shear Stress and Its Role in Atherosclerosis. *JAMA* **1999**, *282* (21), 2035–2042. https://doi.org/10.1001/jama.282.21.2035.
(28) Hammes, M.; Cassel, K.; Boghosian, M.; Watson, S.; Funaki, B.; Coe, F. A Cohort

Study Showing Correspondence of Low Wall Shear Stress and Cephalic Arch Stenosis in Brachiocephalic Arteriovenous Fistula Access. *J. Vasc. Access* **2021**, *22* (3), 380–387. https://doi.org/10.1177/1129729820942048.
(29) Khan, M. O.; Tran, J. S.; Zhu, H.; Boyd, J.; Packard, R. R. S.; Karlsberg, R. P.; Kahn, A. M.; Marsden, A. L. Low Wall Shear Stress Is Associated with Saphenous Vein Graft Stenosis in Patients with Coronary Artery Bypass Grafting. *J Cardiovasc. Transl. Res.* **2021**, *14* (4), 770–781. https://doi.org/10.1007/s12265-020-09982-7.
(30) Crowley, C. J.; Pughe-Sanford, J. L.; Toler, W.; Krygier, M. C.; Grigoriev, R. O.; Schatz, M. F. Turbulence Tracks Recurrent Solutions. *Proc. Natl. Acad. Sci.* **2022**, *119* (34), e2120665119. https://doi.org/10.1073/pnas.2120665119.
(31) Sundin, J.; Bustamante, M.; Ebbers, T.; Dyverfeldt, P.; Carlhäll, C.-J. Turbulent Intensity of Blood Flow in the Healthy Aorta Increases With Dobutamine Stress and Is Related to Cardiac Output. *Front. Physiol.* **2022**, *13*.
(32) Saqr, K. M.; Tupin, S.; Rashad, S.; Endo, T.; Niizuma, K.; Tominaga, T.; Ohta, M. Physiologic Blood Flow Is Turbulent. *Sci. Rep.* **2020**, *10* (1), 15492. https://doi.org/10.1038/s41598-020-72309-8.
(33) Zarins, C. K.; Giddens, D. P.; Bharadvaj, B. K.; Sottiurai, V. S.; Mabon, R. F.; Glagov, S. Carotid Bifurcation Atherosclerosis. Quantitative Correlation of Plaque Localization with Flow Velocity Profiles and Wall Shear Stress. *Circ. Res.* **1983**, *53* (4), 502–514. https://doi.org/10.1161/01.res.53.4.502.
(34) Gusic, R. J.; Myung, R.; Petko, M.; Gaynor, J. W.; Gooch, K. J. Shear Stress and Pressure Modulate Saphenous Vein Remodeling Ex Vivo. *J. Biomech.* **2005**, *38* (9), 1760–1769. https://doi.org/10.1016/j.jbiomech.2004.10.030.
(35) Gusic, R. J.; Petko, M.; Myung, R.; William Gaynor, J.; Gooch, K. J. Mechanical Properties of Native and Ex Vivo Remodeled Porcine Saphenous Veins. *J. Biomech.* **2005**, *38* (9), 1770–1779. https://doi.org/10.1016/j.jbiomech.2005.04.002.
(36) Hyoung-Ho, K.; Young Ho, C.; Sang-Ho, S.; Jeong Sang, L.; Young Hoon, J.; Young Ho, S. Arteriovenous Graft Modeling and Hemodynamic Interpretation. *Open J. Fluid Dyn.* **2012**, *2012*. https://doi.org/10.4236/ojfd.2012.24A040.
(37) Fulker, D.; Simmons, A.; Barber, T. Computational Model of the Arterial and Venous Needle During Hemodialysis. *J. Biomech. Eng.* **2017**, *139* (1). https://doi.org/10.1115/1.4034429.
(38) Chen, B.; Dai, H.; Yang, J.; Tang, K.; Zhang, G.; Xiang, X.; Lin, R.; Huang, Y. Computational Fluid Dynamics Simulation of Hemodynamic Changes in a Hemodialysis Patient with Central Venous Stenosis Treated with Stent. *Semin. Dial.* **2022**, *35* (6), 528–533. https://doi.org/10.1111/sdi.13048.
(39) Pike, D.; Shiu, Y.-T.; Somarathna, M.; Guo, L.; Isayeva, T.; Totenhagen, J.; Lee, T. High Resolution Hemodynamic Profiling of Murine Arteriovenous Fistula Using Magnetic Resonance Imaging and Computational Fluid Dynamics. *Theor. Biol. Med. Model.* **2017**, *14* (1), 5. https://doi.org/10.1186/s12976-017-0053-x.
(40) Varble, N.; Day, S.; Phillips, D.; Mix, D.; Schwarz, K.; Illig, K. A.; Chandra, A. In Vitro Hemodynamic Model of the Arm Arteriovenous Circulation to Study Hemodynamics of Native Arteriovenous Fistula and the Distal Revascularization and Interval Ligation Procedure. *J. Vasc. Surg.* **2014**, *59* (5), 1410–1417. https://doi.org/10.1016/j.jvs.2013.04.055.
(41) Hammes, M.; Moya-Rodriguez, A.; Bernstein, C.; Nathan, S.; Navuluri, R.; Basu, A. Computational Modeling of the Cephalic Arch Predicts Hemodynamic Profiles in Patients

with Brachiocephalic Fistula Access Receiving Hemodialysis. *PLOS ONE* **2021**, *16* (7), e0254016. https://doi.org/10.1371/journal.pone.0254016.
(42) *Creating patient-specific vein models to characterize wall shear stress in hemodialysis population - ScienceDirect*. https://www.sciencedirect.com/science/article/pii/S2001037022004573?via%3Dihub#b0020 (accessed 2023-03-06).
(43) *Increased Inlet Blood Flow Velocity Predicts Low Wall Shear Stress in the Cephalic Arch of Patients with Brachiocephalic Fistula Access | PLOS ONE*. https://journals.plos.org/plosone/article?id=10.1371/journal.pone.0152873 (accessed 2023-04-09).
(44) Albayrak, R.; Yuksel, S.; Colbay, M.; Degirmenci, B.; Acarturk, G.; Haktanir, A.; Karaman, O. Hemodynamic Changes in the Cephalic Vein of Patients with Hemodialysis Arteriovenous Fistula. *J. Clin. Ultrasound JCU* **2007**, *35* (3), 133–137. https://doi.org/10.1002/jcu.20307.
(45) *Vascular Remodeling in Autogenous Arterio-Venous Fistulas by MRI and CFD | SpringerLink*. https://link.springer.com/article/10.1007/s10439-012-0703-4 (accessed 2023-04-09).
(46) Boghosian, M.; Cassel, K.; Hammes, M.; Funaki, B.; Kim, S.; Qian, X.; Wang, X.; Dhar, P.; Hines, J. Hemodynamics in the Cephalic Arch of a Brachiocephalic Fistula. *Med. Eng. Phys.* **2014**, *36* (7), 822–830. https://doi.org/10.1016/j.medengphy.2014.03.001.
(47) *Importance of the Endothelium in Arteriovenous Fistula Outcomes - FullText - American Journal of Nephrology 2016, Vol. 44, No. 6 - Karger Publishers*. https://www.karger.com/Article/FullText/452429 (accessed 2023-04-09).
(48) *COMSOL: Multiphysics Software for Optimizing Designs*. COMSOL. https://www.comsol.com/ (accessed 2023-04-30).
(49) Sage, D.; Unser, M. Teaching Image-Processing Programming in Java, 2003.
(50) Roux, E.; Bougaran, P.; Dufourcq, P.; Couffinhal, T. Fluid Shear Stress Sensing by the Endothelial Layer. *Front. Physiol.* **2020**, *11*.
(51) *How Does My Doctor Know if Dialysis is Working?* https://www.davita.com/treatment-services/dialysis/on-dialysis/how-does-my-doctor-know-if-dialysis-is-working (accessed 2023-04-30).
(52) Anderson, C. B.; Etheredge, E. E.; Harter, H. R.; Codd, J. E.; Graff, R. J.; Newton, W. T. Blood Flow Measurements in Arteriovenous Dialysis Fistulas. *Surgery* **1977**, *81* (4), 459–461.
(53) Kimata, N.; Karaboyas, A.; Bieber, B. A.; Pisoni, R. L.; Morgenstern, H.; Gillespie, B. W.; Saito, A.; Akizawa, T.; Fukuhara, S.; Robinson, B. M.; Port, F. K.; Akiba, T. Gender, Low Kt/V, and Mortality in Japanese Hemodialysis Patients: Opportunities for Improvement through Modifiable Practices. *Hemodial. Int. Int. Symp. Home Hemodial.* **2014**, *18* (3), 596–606. https://doi.org/10.1111/hdi.12142.
(54) Pisoni, R. L.; Arrington, C. J.; Albert, J. M.; Ethier, J.; Kimata, N.; Krishnan, M.; Rayner, H. C.; Saito, A.; Sands, J. J.; Saran, R.; Gillespie, B.; Wolfe, R. A.; Port, F. K. Facility Hemodialysis Vascular Access Use and Mortality in Countries Participating in DOPPS: An Instrumental Variable Analysis. *Am. J. Kidney Dis. Off. J. Natl. Kidney Found.* **2009**, *53* (3), 475–491. https://doi.org/10.1053/j.ajkd.2008.10.043.
(55) Tomo, T.; Larkina, M.; Shintani, A.; Ogawa, T.; Robinson, B. M.; Bieber, B.; Henn, L.; Pisoni, R. L. Changes in Practice Patterns in Japan from before to after JSDT 2013

Guidelines on Hemodialysis Prescriptions: Results from the JDOPPS. *BMC Nephrol.* **2021**, *22* (1), 339. https://doi.org/10.1186/s12882-021-02543-3.